JOM, Vol. 71, No. 8, 2019
https://doi.org/10.1007/s11837-019-03533-5


METALLURGICAL KINETICS

# Isothermal Reduction Kinetics of Chromium-Bearing Vanadium–Titanium Sinter Reduced with CO Gas at 1173 K

SONGTAO YANG,[1,2,3] MI ZHOU,[2,4] XIANGXIN XUE,[2,5] TAO JIANG,[2] and CHANGYU SUN[1]

1.—School of Materials and Metallurgy, University of Science and Technology Liaoning, Anshan 114051, China. 2.—School of Metallurgy, Northeastern University, Shenyang 110819, Liaoning, China. 3.—e-mail: yangsongtao1984@163.com. 4.—e-mail: zhoumineu@163.com. 5.—e-mail: xuexx@mail.neu.edu.cn

The reduction process of chromium-bearing vanadium–titanium sinter (CVTS) was studied under the simulated conditions of a blast furnace at 1173 K, and the kinetics and mineral phases were analyzed. The reduction kinetics of CVTS at different reduction times was studied using a shrinking unreacted core model. The microstructure, mineral phase and variations of the sinter during reduction were observed by x-ray diffraction, scanning electron microscopy and metallographic microscope. Results indicate that the porosity of the CVTS increased with the reduction time and that the reduction rate and degree of the CVTS both improved. Although internal diffusion resistance emerged during the reduction process and gradually increased, the interfacial reduction reaction controlled the entire process and was the rate-limiting factor. Increasing the ratio of microporosity in CVTS is found to be an effective way to improve both the reduction ability and the strength of the CVTS.

## INTRODUCTION

Worldwide reserves of vanadium and titanium magnetite are estimated at over 40 billion tons. Separating and reducing the valuable components of these elements, such as titanium, vanadium and chromite, remain a challenge, in part because these valuable elements are generally fine in texture, and they are scattered and variable in location.[1–7] Much research has been carried out to characterize vanadium and titanium magnetite and to study reductive and thermodynamic steps that might be appropriate for these elements. Qi developed reduction steps for ferrotitanium using $H_2$ and CO, $FeTi_2O_5 \rightarrow Fe_2TiO_4 \rightarrow FeTiO_3$.[8] In Qi's study, the reduction temperature and environment were the two primary control factors. Chu and Shi[9] conducted experiments in reducing different types of vanadium and titanium magnetite using $H_2$ and $CO/CO_2$, and they found that ilmenite and ulvospinel ($Fe_2TiO_4$) could be mutually transformed. Sun et al.[10] focused on a thermodynamic analysis of the phase changes of ferrotitanium and on the interaction among the different phases that occurred during the reduction reaction of ferrotitanium with $H_2$. Prak et al.[11–13] applied a different percentage of a $CO/CO_2$/Ar, $H_2$/Ar and $H_2$/CO mixed gas to reduce ferrotitanium at high temperatures; Prak's study also developed parameters for reducing ferrotitanium under different conditions based on thermodynamic simulations. However, most of this literature was focused on vanadium and titanium magnetite, and few reports have discussed the mechanism of the chromium-bearing vanadium–titanium sinter (CVTS) reduction reaction. Studies generally have focused on Cr-bearing vanadium–titanium magnetite (CVTM) with a highly valuable Cr component. Two major CVTM mining areas are Panzhihua in southwestern China and Chengde in northern China.[14–16] Our own previous work was a fundamental study of the optimal composite ratio for the CVTS before it was fed into a blast furnace.[17,18] The study was focused on the basic characteristics of CVTS and employed a technique of sintering and pelleting rather than focusing on the chemical reactions, reaction mechanisms, rate-limiting factors, etc., inside the blast furnace during the CVTS reduction reaction. The occurrence of a


(Published online May 22, 2019)

CVTS reduction reaction in the upper portion of the blast furnace usually exerts a significant influence on the efficiency of blast furnace production and fuel consumption. Improving the degree of indirect reduction and energy efficiency by means of an enhanced CVTS reduction is important.

This current article studies the reduction reaction of CVTS samples with CO–$N_2$ at 1173 K. The influence of porosity, reduction thermodynamics and the mineral phase structure on the behavior of the CVTS during the reduction process was explored. It was found that these factors were critical to improving reduction efficiency and energy efficiency in the CVTM sintering process.

## MATERIALS AND METHODS

CVTM is a mixture comprising four single chromium-bearing vanadium–titanium iron ores exploited from four CVTM mines in Chengde District, Hebei Province, China. The CVTS was prepared according to the conditions of the Chengde Jianlong Steel Co. The mixture had a basicity of 1.9 and a carbon percentage of 3.6%. The granulated mixture was first sintered for 2 min at < 1373 K in a sinter pot. When the sintered sample reached the sintering temperature, the sample was removed from the sinter pot and cooled to ambient temperature for 10 min. The sintering tests included the proportioning, mixing, granulation, ignition, sintering, cooling, crushing and treatment of the cooled sinter. After the crushing of the sinter screening, a diameter of 10–12.5 mm CVTS was obtained for the reduction of the experimental raw materials. The chemical composition of the CVTS is shown in Table I.

Figure 1 shows the reduction experiment equipment; its reaction tube has an inner diameter of 75 mm. The equipment can record changes in the sample weight during the heating process under different heating mechanisms and conditions. Because the material interchange is forced by the countercurrent energy during the sintering process, the iron ore is reduced from the top to the bottom of the blast furnace. Therefore, the selection of the gas reduction and test temperature reference of the iron wustite reaction was more cohesive in the 1173 K zone in the upper region of the atmosphere and temperature conditions of the blast furnace.[19]

The resolution of the electronic balance is 0.01 g; 500 g of the CVTS sample was placed on the platform of the reaction tube, which was heated to 1173 K under the protection of 5 l/min $N_2$. The tube temperature was held at 1173 K with the protection of 15 l/min $N_2$ for 30 min. The reducing gas mixture (70 vol.%CO–30 vol.%$N_2$) was introduced to the reactor. The reduction reaction was maintained for 60, 90, 120, 150 and 180 min. Pumping of the reaction gas was stopped when the reaction time was completed. Then, during the cooling process, the flow of 5 l/min $N_2$ gas was pumped to the reactor until the samples were cooled to room temperature.

The reduction degree ($R_t$) was determined with reference to Fe(III) and was calculated using Eq. 1.

$$R_t = \left(\frac{0.111w_1}{0.430w_2} + \frac{m_1 - m_t}{m_0 \times 0.430w_2} \times 100\right) \times 100 \quad (1)$$

Here, $m_0$ is the mass of the sample (g), $m_1$ is the mass of the sample before reduction (g), $m_t$ is the mass of the sample reduction for $t$ minutes (g), $w_1$ is the FeO content of the sample (%), and $w_2$ is the TFe content (%) of the sample.

The sinter porosity tests were performed on the sinter, and the instrument used was the AutoPore IV 9510 Mercury Injection Apparatus, manufactured by Micromeritics (Atlanta, GA, USA). The sinter samples obtained from each experiment were mounted on an epoxy resin, polished with coarse sandpaper, smoothed onto a frosted glass panel and characterized with a JEOL S-3400 N scanning electron microscope (SEM) (JEOL Ltd., Tokyo, Japan). Mineral phase microscope analysis data were obtained from the average statistical area of each mineral and the total observational scope area, which was characterized with an image analyzer (Cambridge Q500; Leica Microsystems).

## EXPERIMENTAL RESULTS

### Degree of Reduction and Porosity Change

Figure 2 shows the reduction curve and porosity of the CVTS at five different reaction times. The five curves almost overlap, which demonstrates that the results were consistent for all samples and met the requirement for post-processing. The degree of reduction reached 72.8% rather than 100%; the 100% threshold is a theoretical goal for an experiment in which the reduction reaction occurs at an equilibrium state. Our results reflect the reduction of the titanomagnetite, wustite and ulvospinel solid solutions that were generated in the later stages of the reduction process; it is difficult to reduce these solutions. Meanwhile, it is possible to produce cementite. The combination of the two results

**Table I. Chemical composition of CVTS (mass%)**

| TFe | FeO | CaO | $SiO_2$ | MgO | $Al_2O_3$ | $V_2O_5$ | $TiO_2$ | $Cr_2O_3$ |
|---|---|---|---|---|---|---|---|---|
| 53.68 | 10.59 | 10.40 | 5.47 | 3.08 | 2.19 | 0.20 | 1.78 | 0.23 |

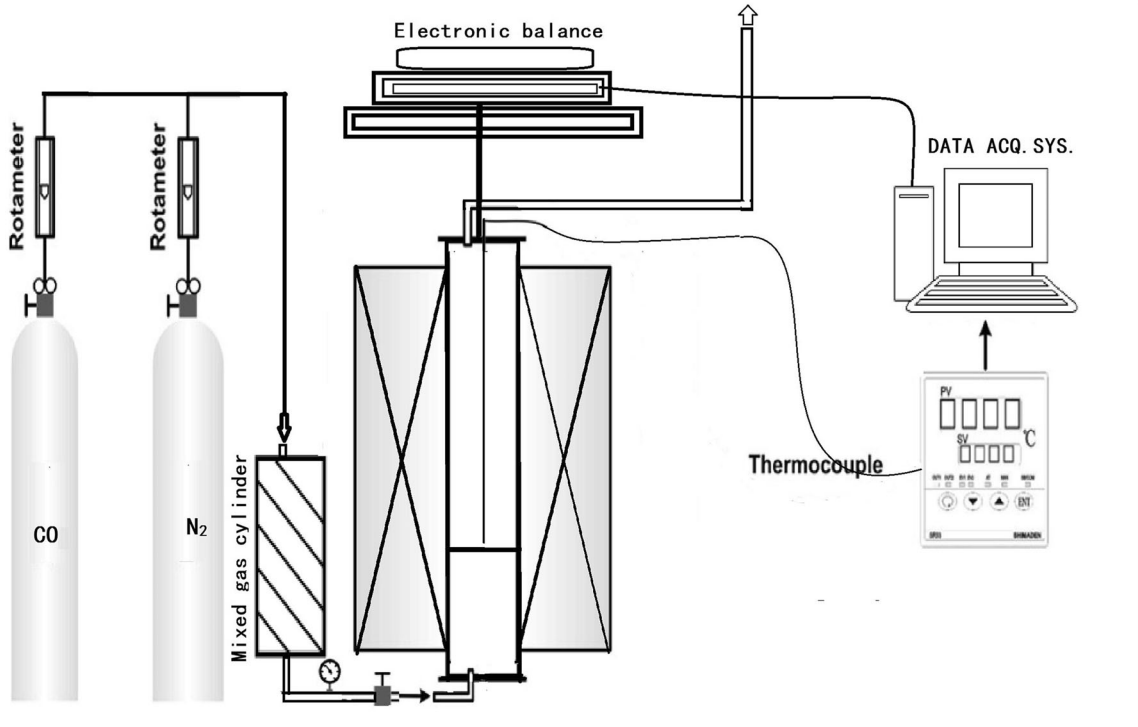


Fig. 1. Schematic of the experimental system.

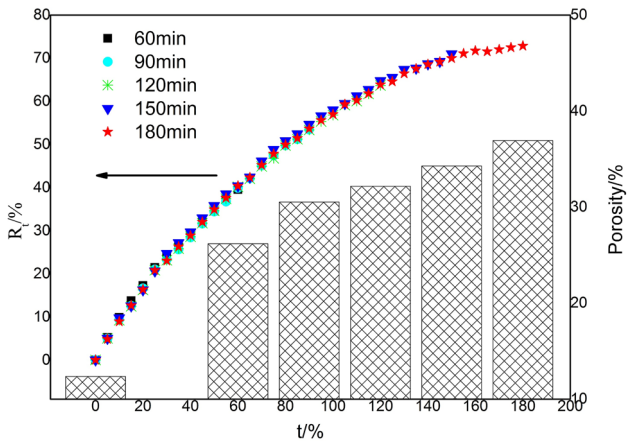


Fig. 2. Reduction curves and porosity of CVTS at different reaction times.

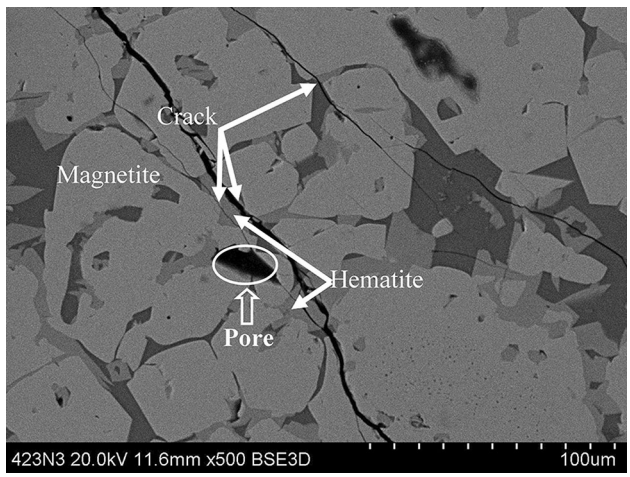


Fig. 3. SEM photographs of CVTS reaction products at $m_t$ = 60 min.

reflects the above results. The chemical responses of the reduction processes are as follows:

$$2CO + O_2 = CO_2(g) \tag{2}$$

$$FeTiO_3 + FeO = Fe_2TiO_4 \tag{3}$$

$$mFe_3O_4 \cdot n[(Fe,\ Mg,\ Mn)_2TiO_4] \cdot pFeV_2O_4 + CO = 3mFeO + n[(Fe,\ Mg, Mn)_2TiO_4 \cdot pFeV_2O_4 + \ CO_2(g) \tag{4}$$

$$3Fe + C = Fe_3C \tag{5}$$

Figure 2 shows that the porosity and degree of reduction both increased with the increase of reduction time. The porosity increased from 12.36% to 36.94% at a reduction time of 180 min. The increment of increase was 118%, 147%, 160%, 177%, and 199% at reduction times of 60 min, 90 min, 120 min, 150 min, and 180 min, respectively. Porosity showed the largest improvement during the initial reduction stage, when the hematite began to be reduced and expanded because many cracking and porous structures were created. The cracking and porous structures opened a large number of closed pores, which improved porosity further

(Fig. 3). The reaction $Fe_2O_3 \rightarrow Fe_3O_4$ decreased and $Fe_3O_4 \rightarrow Fe_xO$ increased in the middle stage of the reaction. The expansion of the volume slowed, and the release of closed pores and improvement of porosity also slowed in this stage. At the final stage, the only reduction reaction that occurred was $Fe_xO \rightarrow Fe$, and the volume continued to shrink. The reduced metallic iron became nucleated and grew. More spaces were released inside the sinter, leading to improved porosity. Hence, porosity continued to increase during the entire reduction process because of different mechanisms. In the early stage, expansion was caused by cracking. In the later stage, expansion was caused by shrinkage. The improvement of porosity increased the interaction boundary, accelerated the reduction rate and improved the dynamic behavior, which resulted in a higher degree of CVTS reduction.

## Reduction Dynamics Analysis

The mechanism of iron ore reduction has been studied for many years, and in these studies, a shrinking unreacted core model was the most widely used.[20,21] Mineralogic analysis has produced evidence of the sinter reduction $Fe \rightharpoonup FeO \rightharpoonup Fe_3O_4 \rightharpoonup Fe_2O_3$ occurring from the exterior to the interior for different degrees of reaction.[22] The resistances of the reduction reaction consisted of external diffusion, chemical reaction and diffusion through the product layer, based on the shrinking unreacted core model theory. The production layer was thin when reduction began, and the gas diffusion resistance in the production layer was slight. The chemical reaction rate was rapid at the high temperature (1173 K), so the interfacial chemical reaction resistance was small. Gas flow was low, and the mass transfer across the gas boundary was appreciable in the current experiment. The three-step mixture control model was used to process the data.

Under the conditions of constant temperature and pressure, the reduction of $Fe_2O_3$ with CO can be expressed as the following equation, if carried out in conformity with the interfacial un-reacted core model.

$$Fe_xO(s) + CO(g) = xFe(s) + CO_2(g) \quad (6)$$

To obtain the corresponding reaction rate equation, at the time of derivation, it is assumed that the reaction was a quasi-steady process without regard to volume changes of the ore pellet during the reaction. In addition, temperature was uniform inside the sinter, and its reduction reaction was level-1 reversible. In line with the above assumptions, the un-reacted core model may be used to establish the reduction reaction kinetics equation.

In the process of vanadium titanium sinter reduction, CO with a concentration of $C_{Ab}$ (mol/m$^3$) flowed toward the surface of the vanadium titanium sinter at a flow rate of $u_0$ (l/min) and diffused to the internal reaction interface of the sinter after passing through a gas-phase boundary layer and a reduced iron layer around the sinter to perform a chemical reaction at the interface. Concentration of CO on the surface of sinter was $C_{As}$, while it was $C_{Ai}$ in the reaction boundary, and the equilibrium concentration of reaction was $C^*$.

When $dn(CO)/dt$ of CO concentration is considered to be the reduction rate of $Fe_xO$, it can be expressed as follows in accordance with the reduction reaction equation of $Fe_xO$:

$$v = -\frac{dn[O(Fe_xO)]}{dt} = -\frac{dn(CO)}{dt} \quad (7)$$

where $t$ is the reaction time when the radius of the un-reacted core reaches $r$.

When the reduction reaction process is composed of three links, which is the external diffusion of the CO at the boundary layer of the gas phase, the rates of the internal diffusion of CO within the reduced iron layer and of the interfacial chemical reaction can be derived by the principle of steady state.

If the three links are carried out in steady state, $v_1 = v_2 = v_3$. According to the above relationship, the interfacial concentration $C$, which cannot be measured, is eliminated, so the overall reaction rate can be obtained as follows.

$$v = -\frac{dn}{dt} = \frac{4\pi r_0^2 (C_{Ab} - C^*)}{\frac{1}{\beta} + \frac{r_0}{De}\cdot\frac{r_0 - r}{r} + \frac{K}{k(1+K)}\cdot\frac{r_0^2}{r^2}} \quad (8)$$

where $r_0$ is the original radius of FeO, $\beta$ is the mass transfer coefficient, $De$ is the effective diffusion coefficient, $r$ is the radius of un-reacted core, $K$ is the reaction equilibrium constant, and $k$ is the reaction rate constant.

The un-reacted core radius $r$ is replaced by the $R_t$ of the sinter, and $R_t$ is set to $x$:

$$r = r_0(1 - x)^{1/3} \quad (9)$$

After Eq. 9 is substituted into Eq. 7, we can obtain the equation below.

$$v = -\frac{dn}{dt} = \frac{4\pi r_0^2 (C_{Ab} - c^*)}{\frac{1}{\beta} + \frac{r_0}{De}[(1 - x)^{-1/3} - 1] + \frac{K}{k(1+K)}\cdot(1 - x)^{-2/3}} \quad (10)$$

To acquire the integral equation of the reaction rate, the variable $n$ needs to be eliminated from Eq. 10. If the rate of change of oxygen's mole number in the sinter is used to denote the reduction rate, we can obtain:

$$-\frac{dn[O(Fe_xO)]}{dt} = -\frac{d}{dt}\left(\frac{4}{3}\pi r^3 \rho_0\right) = -4\pi r^2 \rho_0 \cdot \frac{dr}{dt} \quad (11)$$

where $\rho_0$ is the density of $Fe_xO$.

By substituting Eq. 9 into Eq. 11, we can achieve the following equation:

$$-\frac{\mathrm{d}n[\mathrm{O(Fe}_x\mathrm{O)}]}{\mathrm{d}t} = -4\pi r_0^2(1-x)^{2/3}\rho_0 \cdot \frac{\mathrm{d}}{\mathrm{d}t}[r_0(1-x)^{1/3}] = \frac{4}{3}\pi r_0^3\rho_0 \cdot \frac{\mathrm{d}x}{\mathrm{d}t} \tag{12}$$

For Reaction Eq. 7, the equation is:

$$-\frac{\mathrm{d}n(\mathrm{CO})}{\mathrm{d}t} = -\frac{\mathrm{d}n[\mathrm{O(Fe}_x\mathrm{O)}]}{\mathrm{d}t} \tag{13}$$

Therefore, Eq. 10 is equal to Eq. 12, and it can be simplified as:

$$\frac{\rho_0 r_0}{3(C_{\mathrm{Ab}}-c^*)}\left\{\frac{1}{\beta}+\frac{r_0}{De}[(1-x)^{-1/3}-1] + \frac{K}{k(1+K)}\cdot(1-x)^{-2/3}\right\}\mathrm{d}R = \mathrm{d}t \tag{14}$$

When $t = 0 \sim t$, Eq. 14 can be solved in the following way within the corresponding boundary of $x = 0 \sim x$ through integration:

$$t = \frac{\rho_0 r_0}{C_{\mathrm{Ab}}-c^*}\left\{\frac{x}{3\beta}+\frac{r_0}{6De}\left[1-3(1-x)^{2/3}+2(1-x)\right] + \frac{K}{k(1+K)}\left[1-(1-x)^{1/3}\right]\right\} \tag{15}$$

It also can be indicated as the following equation in a simpler manner:

$$t = \frac{\rho_0 r_0}{C_{\mathrm{Ab}}-c^*}f(x) \tag{16}$$

Equation 15 is the mathematical expression for the reduction time and reduction rate of the sinter, where the first item represents the diffusion resistance on the gas-phase boundary layer, the second item refers to the diffusion resistance within the reduced iron layer, and the third item is the interfacial chemical reaction resistance. Influences of the relative magnitude of these resistances on reduction time vary with changes in the properties and reaction conditions of sinter. Meanwhile, the restrictive links of the reduction process also change correspondingly.

According to differences in the relative magnitudes of $\beta$, $De$ and $k$, the rate equation can be further obtained to provide that only one of the above restrictive links plays a limited role.

Mixed constraints: $De \approx k$ and $De \ll \beta$

$$t = \frac{\rho_0 r_0}{C_{\mathrm{Ab}}-c^*}\left\{\frac{r_0}{6De}\left[1-3(1-x)^{\frac{2}{3}}+2(1-x)\right] + \frac{K}{k(1+K)}\left[1-(1-x)^{\frac{1}{3}}\right]\right\} \tag{17}$$

Equation 17 can be simplified as follows:

$$t\Big/[1-(1-x)^{1/3}] = m[1+(1-x)^{1/3}-2(1-x)^{2/3}]+n \tag{18}$$

where $m = \frac{\rho_0 r_0^2}{6De(c^0-c^{\mathrm{equilibrium}})}$, $n = \frac{\rho_0 r_0 K}{k(1+K)(c^0-c^{\mathrm{equilibrium}})}$

The line with slope $m$ and interception $n$ may be obtained for $t\Big/[1-(1-x)^{1/3}]$ and $1+(1-x)^{1/3}-2(1-x)^{2/3}$. $De$ and $k$ are calculated as shown in Fig. 4.

The line aggression function $Y = F(X)$ for $t/[1-(1-x)^{1/3}]$ and $1+(1-x)^{1/3}-2(1-x)^{2/3}$ is obtained from Fig. 4.

$$Y = 152.18X + 313.50 \tag{19}$$

For Reaction Eq. 18, the equation is:

$$De = \frac{\rho_0 r_0^2}{6m(C_{\mathrm{Ab}}-c^*)}, \quad k = \frac{\rho_0 r_0 K}{n(1+K)(C_{\mathrm{Ab}}-c^*)}$$

For $\Delta_r G_m = \Delta_r G_m^\theta + RT\ln K = 0$, its equation is $K = \exp(-\frac{\Delta_r G_m^\theta}{RT})$

$$C_{\mathrm{Ab}} - c^* = \frac{p'}{RT}[1-1\times\frac{\varphi(CO)_{(\text{平})}}{100}]^3 \tag{20}$$

Therefore,

$$f_i = \frac{r_0}{De}\cdot\frac{r_0-r}{r} = \frac{r_0}{De}\left[(1-x)^{-1/3}-1\right] \tag{21}$$

$$f_r = \frac{K}{k(1+K)}\cdot\frac{r_0^2}{r^2} = \frac{K}{k(1+K)}\cdot(1-x)^{-2/3} \tag{22}$$

Interfacial chemical reaction resistance ratio: $R_{\mathrm{r}} = \frac{f_r}{f_r+f_i}$

Internal diffusion resistant ratio: $R_{\mathrm{i}} = 1 - R_{\mathrm{r}}$

The curves of the two resistance ratios with respect to the degree of reduction under different reduction temperatures are shown in Fig. 5 by means of the interfacial chemical reaction resistance ratio $R_{\mathrm{r}}$ and the internal diffusion resistant ratio $R_{\mathrm{i}}$.

Figure 5 shows that the interfacial reduction reaction was dominant during the initial stage in a reduction environment of 30% CO + 70% $N_2$. With the further processing of the reduction reaction and the thinning of the production layer, the internal diffusion resistance began to increase quickly. However, the interfacial chemical reaction continued to control the reduction, and this is considered to be the rate-limiting factor in this experiment.

## Mineralogic Structure Analysis

Figures 6 and 7 show, respectively, the x-ray diffraction (XRD) pattern of the CVTS reaction products at different reaction times and the mineral compositions. Magnetite and hematite are both main composites and co-exist with binder phases such as calcium ferrite, silicate, glassy mass, etc.,

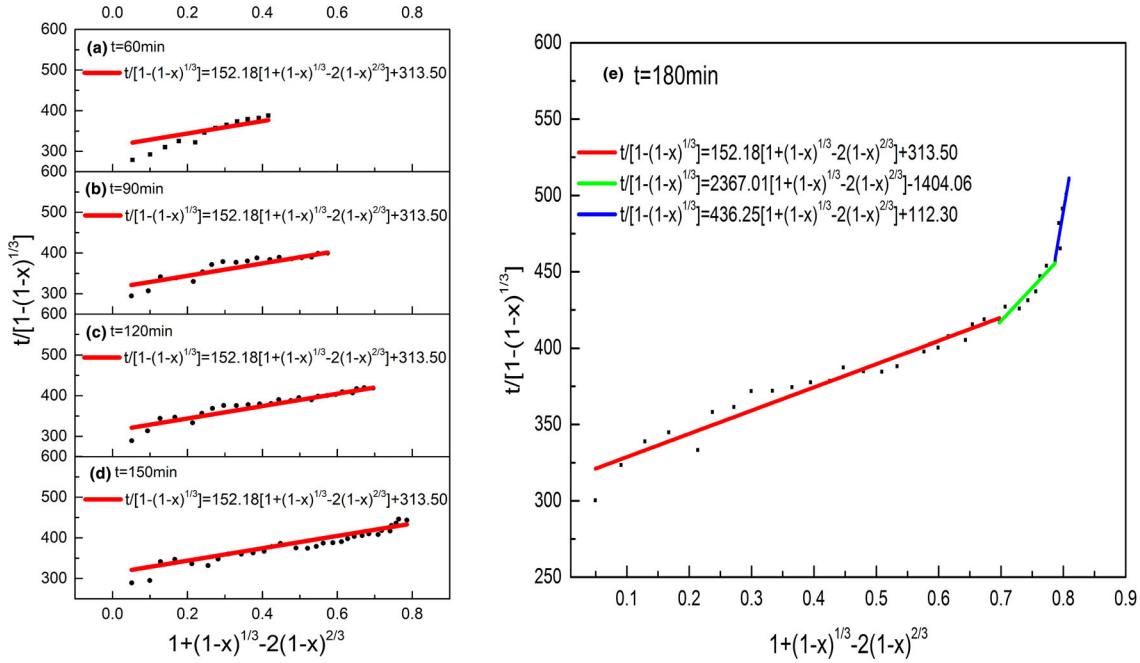


Fig. 4. The graph of $t/[1-(1-x)^{1/3}]$ and $1+(1-x)^{1/3}-2(1-x)^{2/3}$: (a) $m_t$ = 60 min; (b) $m_t$ = 90 min; (c) $m_t$ = 120 min; (d) $m_t$ = 150 min; (e) $m_t$ = 180 min.

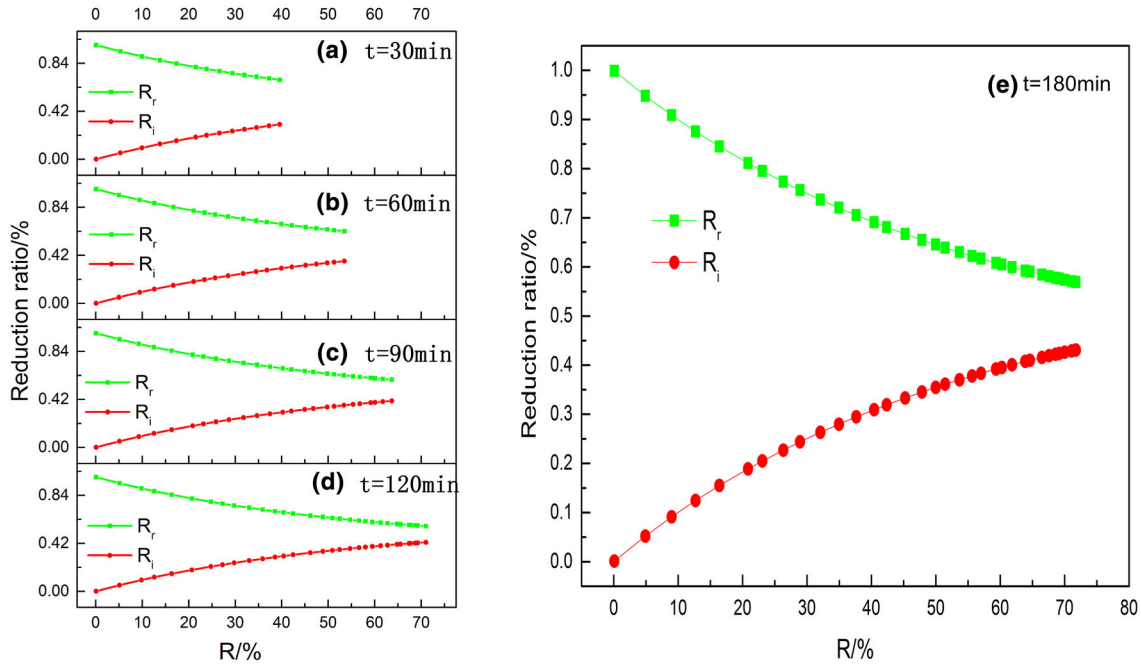


Fig. 5. Change in the two resistance rates according to reduction rate at 1173 K: (a) $m_t$ = 60 min; (b) $m_t$ = 90 min; (c) $m_t$ = 120 min; (d) $m_t$ = 150 min; (e) $m_t$ = 180 min.

before the reduction. The amounts of magnetite, hematite, calcium ferrite and silicate were gradually reduced and replaced by metallic iron and wustite during the reduction reaction, while the amount of perovskite showed no obvious change at this stage. The total amount of metallic iron and wustite peaked from 90 min to 120 min. Also, the mineral composites of the CVTS samples remained unchanged after 120 min when the reduction reaction was almost complete.

Figure 8 shows the mineralogic microstructures of the CVTS samples at different reduction times. The CVTS was reduced from high to low valence, and from the exterior to the interior of the sinter

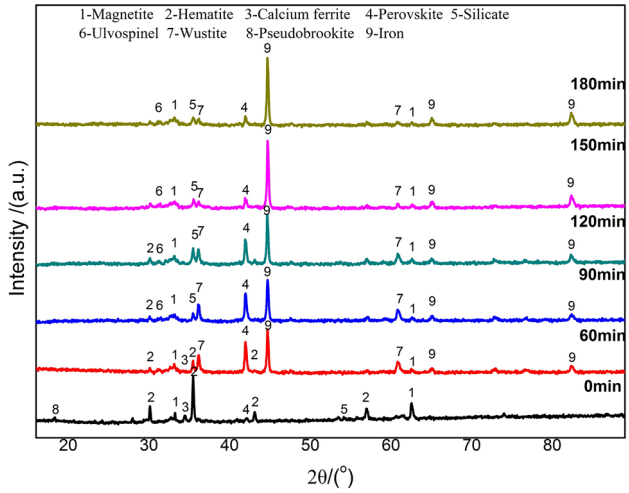


Fig. 6. XRD of CVTS reaction products at different reduction times.

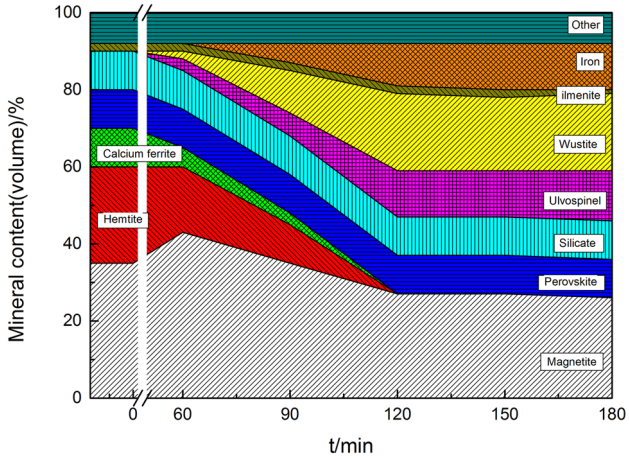


Fig. 7. Mineral composition distribution of CVTS reaction products at different reaction times.

samples, in a stepwise fashion. The CVTS consisted of hematite, magnetite, perovskite and calcium ferrite before the reduction reaction. Hematite and magnetite existed in the forms of euhedral, subhedral and anhedral crystals, while the calcium ferrite displayed dendritic and tabular crystal structures (Fig. 8a). The cores of the CVTS samples retained the original morphology and composites after approximately 60 min of the reduction reaction. In terms of the reduction reaction of hematite-magnetite and calcium ferrite-magnetite, it is found that the magnetite began from the exterior boundary of the samples. Figure 8b clearly shows the reaction boundary when the reduction gas diffused to the reaction boundary and ignited the hematite-magnetite and calcium ferrite-magnetite reaction. The volume of hematite and calcium ferrite decreased in the early reduction stages compared with the original CVTS samples, which are shown in Fig. 7. Hematite has a better reduction ability than calcium ferrite, which means that the former composite has a higher reduction rate than the latter. On the other hand, the large pore and porous structure of the hematite is beneficial for gas diffusion and reduction dynamics, and these characteristics further accelerated the reduction of the hematite. Although magnetite was reduced to wustite, the newly produced magnetite exceeded the amount of reduced magnetite.

Figure 8c and d shows that all of the hematite and calcium ferrite was gradually reduced to magnetite in the samples at 60–120 min, while a large amount of the magnetite was reduced to wustite and ulvospinel at this temperature interval. Thus, the amounts of magnetite, hematite and calcium ferrite were found to have good reduction ability that was gradually reduced and replaced by metallic iron and wustite, both of which are hard to reduce. This evolution of the composites matches the tendency of change in the reduction ratio of CVTS.

Figure 8e and f shows that some of the floating bodies were gradually reduced to metal iron, and the structure changes in most of the regions occurred because of the formation of uniform metallic iron and the growth of metallic iron nucleation. The other minerals in the sinter were almost unchanged, indicating that the reduction of other minerals after reaction for 120 min was stagnant.

## DISCUSSION

The reduction of iron oxide by CO is a typical gas and solid uncatalyzed reaction. It is controlled by the internal diffusion of the gas, as well as by external diffusion and a chemical reaction; these are the slowest reactions that control the reduction rate.[17,18] Reactions usually have different rate-limiting factors for a typical reduction reaction. Reduction reactions are dependent on the physical and chemical properties of the samples as well as on the conditions of the reduction environment.[23] The rate-limiting factors vary in the different stages of the CVTS reduction process because of the non-uniform structures of CVTS in different regions of the samples. In the early reduction stage, calcium ferrite is reduced to magnetite. The newly produced magnetite is more porous than the calcium ferrite, and cracking occurs at the same time. The reduction gas diffuses along the cracks and enters into the pores in which the reduction reaction first occurred; it then gradually expands to surrounding areas (Fig. 8a). Therefore, the interfacial chemical reaction is the rate-limiting factor in the early stages of the CVTS reduction reaction.

In the middle and later stages of the reduction, wustite begins to be produced. There is a clear reduction reaction boundary between the wustite and the metallic iron, because wustite is dense and cannot easily be penetrated by the reduction gas when gas moves through the pores. Many micropores become distributed inside the sinter in the middle and later stages of the reduction. The reduction gas can easily penetrate these micropores,

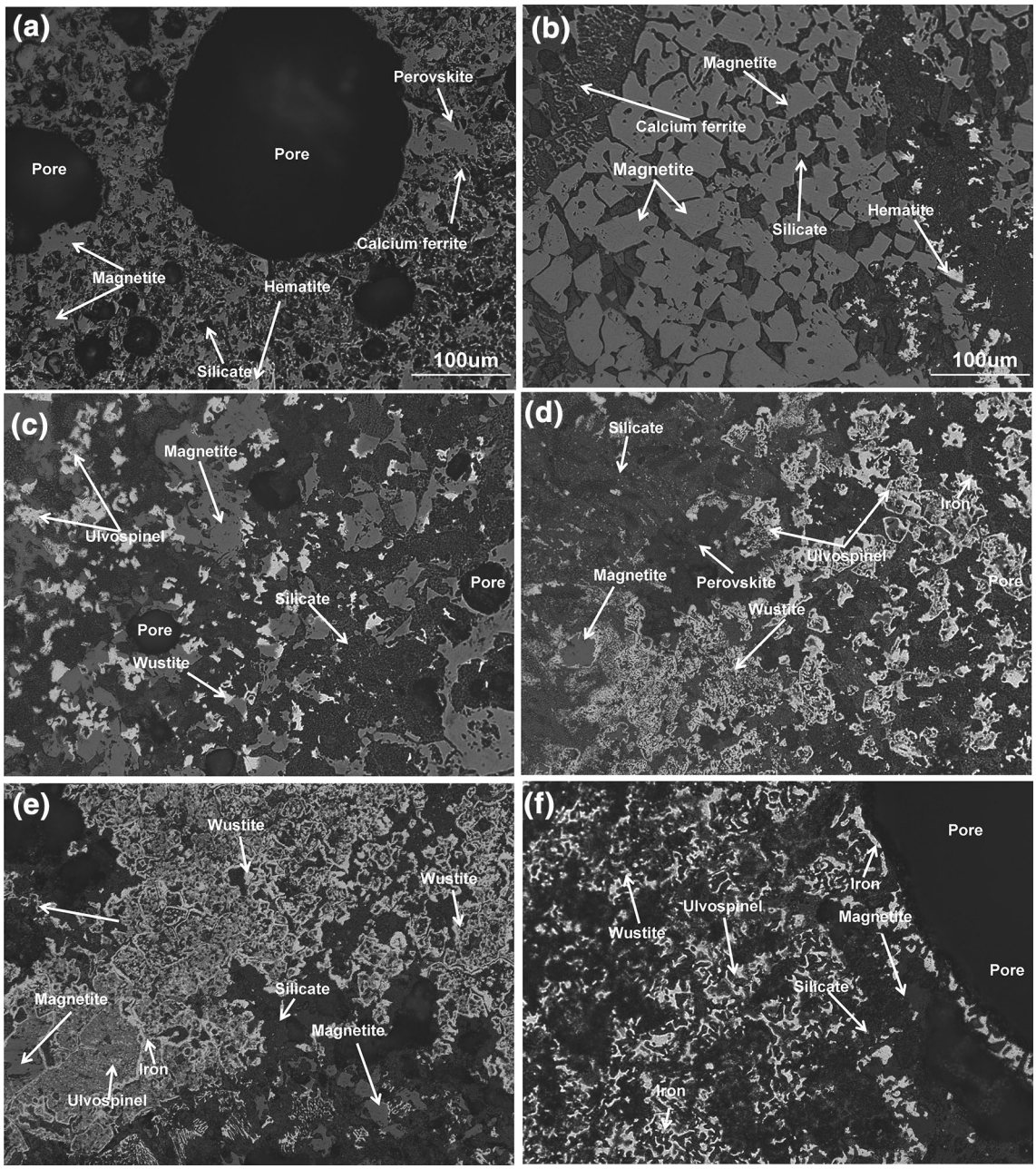


Fig. 8. Micrograph of CVTS reaction products at different reduction times: (a) $m_t$ = 0 min; (b) $m_t$ = 60 min; (c) $m_t$ = 90 min; (d) $m_t$ = 120 min; (e) $m_t$ = 150 min; (f) $m_t$ = 180 min.

causing the reduction process to occur dispersedly and efficiently at these points. The rate-limiting factor in the middle and later stages is the combination of interfacial chemical reactions and internal diffusion (Fig. 8d). Analysis of the mineral phase transformation and the microstructural results demonstrates that predictions about the rate-limiting factor in the reduction reaction that were used to evaluate the shrinking unreacted core model are credible.

The interfacial chemical reaction is the main rate-limiting factor across the entire CVTS reduction process. Increasing the content of micropores in CVTS can improve the kinetic conditions of the CVTS reduction reaction, which is beneficial to the reduction reaction. Hence, increasing the percentage of micropores in the CVTS is critical to improving the reduction and strength of the CVTS.

## CONCLUSION

(1) This study found that the interfacial chemical reaction was dominant in the CVTS reduction process with 30 vol.% CO + 70 vol.% $N_2$ at a temperature of 1173 K in the initial stage. Internal diffusion began to achieve a higher ratio with further processing of the reduction and the use of

thinner reduction products. However, the interfacial chemical reaction was still the prominent rate-limiting factor in the experiment described in this article.

(2) To increase the content of micropores in the CVTS, especially to increase the microporosity of the sinter—which is more advantageous to the reduction, because it increases the reaction boundaries—we accelerated the reduction rate to improve the dynamic conditions. Hence, increasing the percentage of micropores in the CVTS was found to be a critical and effective way to improve the reduction and strength of the CVTS.

## ACKNOWLEDGEMENTS

This research was financially supported by the Programs of the National Natural Science Foundation of China (Nos. 51604065, 51674084, 51174051 and 51574082), the National Basic Research Program of China (973 Program) (No. 2013CB632603), the Fundamental Funds for the Central Universities (Nos. N172507012 and 150202001), the Program of the National Natural Science Foundation of Liaoning Province (20170540316) and the National Key Technology Research and Development Program (No. 2015BAB19B02), the Youth Fund of University of Science and Technology Liaoning (No. 2018QN05).

## REFERENCES

1. H.G. Du, *Principle of Smelting Vanadium–Titanium Magnetite in the Blast Furnace* (Beijing: Science, 1996), p. 1.
2. J.X. Liu, G.J. Cheng, Z.G. Liu, and X.X. Xue, *Steel Res. Int.* 86, 808 (2015).
3. S.T. Yang, Y.L. Gan, X.X. Xue, and B. Li, *Ironmak. Steelmak.* 45, 959 (2018).
4. S.T. Yang, M. Zhou, T. Jiang, and X.X. Xue, *Int. J. Miner. Met. Mater.* 23, 1353 (2016).
5. M. Gan, Z.Y. Ji, X.H. Fan, W. Lv, R.Y. Zheng, X.L. Chen, S. Liu, and T. Jiang, *Powder Technol.* 333, 385 (2018).
6. G.J. Wong, X.H. Fan, M. Gan, Z.Y. Ji, X.L. Chen, Z.Y. Tian, and Z.Z. Wang, *Powder Technol.* 342, 873 (2019).
7. M. Gan, Z.Y. Ji, X.H. Fan, X.L. Chen, R.Y. Zheng, L. Gao, G.J. Wang, and T. Jiang, *Powder Technol.* 328, 122 (2018).
8. D.G. Qi, *Chin. J. Process Eng.* S1, 27 (1979).
9. S.B. Chu and S.T. Shi, *Iron Steel* 16, 13 (1981).
10. K. Sun, Y.Y. Ma, G.C. Bai, and F.J. Liu, *Chin. J. Nonferrous Met.* 8, 390 (1998).
11. E. Park and O. Ostrovski, *ISIJ Int.* 44, 74 (2004).
12. E. Park and O. Ostrovski, *ISIJ Int.* 44, 999 (2004).
13. E. Park and O. Ostrovski, *ISIJ Int.* 43, 1316 (2003).
14. M. Zhou, S.T. Yang, T. Jiang, and X.X. Xue, *Ironmak. Steelmak.* 42, 217 (2015).
15. M. Zhou, S.T. Yang, T. Jiang, and X.X. Xue, *JOM* 67, 1203 (2015).
16. S.T. Yang, M. Zhou, T. Jiang, and X.X. Xue, *Miner. Basel* 7, 210 (2017).
17. S.T. Yang, M. Zhou, T. Jiang, and X.X. Xue, *Trans. Nonferrous Met. Soc.* 25, 2087 (2015).
18. M. Zhou, S.T. Yang, T. Jiang, X.X. Xue, and W.J. Zhang, *Metall. Res. Technol.* 113, 612 (2016).
19. X.L. Wang, *Iron and Steel Metallurgy (Ironmaking)* (Beijing: Metallurgical Industry Press, 2000), p. 77.
20. A.A. El-Geassy, *Ironmak. Steelmak.* 26, 41 (1999).
21. A.A. El-Geassy, *ISIJ Int.* 36, 1344 (1996).
22. Y. Zhao, K. Wu, W. Pan, and Q.H. Liu, *J. Northeast. Univ. Nat. Sci.* 34, 1282 (2013).
23. M.I. Nasr, A.A. Omar, M.H. Khedr, and A.A. El-Gesaay, *ISIJ Int.* 35, 1043 (1995).